5-1-2008

Tomographic Imaging of Airglow from Airborne Spectroscopic Measurements

D. Scott Anderson
University of Illinois at Urbana-Champaign

Gary Swenson,
University of Illinois at Urbana-Champaign

Farzad Kamalabadi
University of Illinois at Urbana-Champaign

Alan Liu
Embry Riddle Aeronautical University - Daytona Beach, liuz2@erau.edu

Tomographic imaging of airglow from airborne spectroscopic measurements

D. Scott Anderson,* Gary Swenson, Farzad Kamalabadi, and Alan Liu

University of Illinois at Urbana–Champaign, Department of Electrical and Computer Engineering, Urbana, Illinois 61801, USA

*Corresponding author: dscottanderson@gmail.com

Received 24 October 2007; revised 1 February 2008; accepted 20 March 2008;
posted 20 March 2008 (Doc. ID 88970); published 30 April 2008

A description is given of the methodology based on a single, aircraft-mounted spectroscopic imager to tomographically reconstruct airglow perturbations induced by atmospheric gravity waves. In this configuration, the imager passes under the airglow structure to gather multiple-angle views of the wave structure in a relatively short amount of time. Under the assumption that the airglow structure does not change significantly during the acquisition interval, the data can be tomographically inverted to estimate the 2D (horizontal–vertical) airglow structure. We develop an inversion strategy for this image formation task and illustrate its applicability by inverting time-sequential imaging data taken from different vantage points during the ALOHA-93 campaign to reconstruct atmospheric gravity wave structures.

OCIS codes: 010.0280, 100.3010, 280.4991, 010.7350.

1. Introduction

As a continuous and dynamic fluid, the Earth's atmosphere is able to support propagating waves called atmospheric gravity waves (AGWs), which have been shown to play an important role in the momentum and thermal balance of the upper atmosphere [1–3]. AGWs, also called buoyancy waves, are able to propagate both horizontally and vertically, as illustrated by the diagram of a simple, monochromatic plane gravity wave in Fig. 1. As the figure suggests, AGWs have an intrinsic phase speed, c_i, which is related to the horizontal and vertical wavelength of the wave. As AGWs propagate, they transport energy and momentum from one part of the atmosphere to another. Eventually this momentum is deposited into the atmosphere through viscous processes, or the waves become so large in amplitude that they break and generate turbulence. As a result, there is great interest in characterizing AGWs in the mesosphere to determine their specific impact in contributing to the atmospheric dynamics.

The mesosphere is a region in the atmosphere that is home to several chemiluminescent processes called airglow emissions. These emissions are stratified by height and confined to an altitude layer. As gravity waves pass through this layer, they displace key emission constituents along the phase fronts such that the intensity of the airglow is spatially modulated by the wave (in both the horizontal and the vertical directions). In Fig. 2, the vertical profile of a standard, unperturbed hydroxyl (OH) airglow process (as modeled in [4]) is shown by the thick solid curve [4,5]. The thin solid curves in the figure represent several instances of the profile as it is perturbed 5% by an AGW with a vertical wavelength of 25 km.

Relatively recently, scientific-grade CCD sensors have been used to directly measure AGW parameters by imaging airglow perturbations from the ground (e.g., [6,7]). Typically for this method, different temporal instances of these airglow images are subtracted to remove the ambient emission brightness and to highlight the propagating wave structure. This time-differencing effectively reduces the perturbed profiles represented as the thin solid curves in Figure 2 to the time-differenced profiles represented by the thin dashed curves. Note that the

0003-6935/08/132510-10$15.00/0

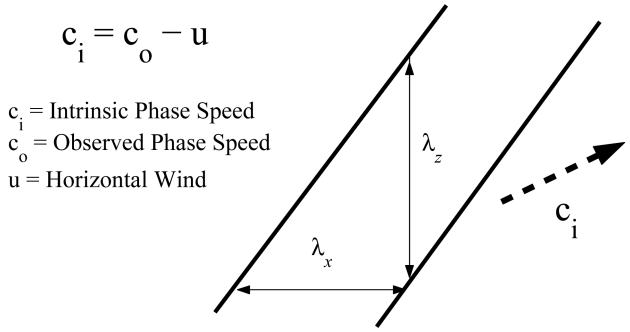

Fig. 1. Diagram of the phase fronts of a plane AGW. The propagation speed of the wave relative to the ground is dependent on the mesospheric wind and the intrinsic phase speed of the wave.

time-differenced profiles can be represented as a monochromatic wave enveloped by the time-difference envelope shown as the thick dashed curve.

Ultimately, the observations of AGW-induced airglow perturbations can be used to estimate the vertical flux of the wave momentum (e.g., [4,7–9]). The intrinsic wave parameters required for estimating the momentum flux are the horizontal wavelength (λ_x), vertical wavelength (λ_z), intrinsic phase speed (c_i), and the wave amplitude. An atmospheric wave dispersion relation exists [1] that relates λ_x, λ_z, and c_i such that any two of these can be used to find the third. Because the raw data from airglow imagers (which typically have a hemispherical field of view) represent a projection of the three-dimensional field onto the two-dimensional image plane, the only intrinsic wave parameter that can be directly measured from imagery with a single-layer observation is λ_x. The vertical wavelength is traditionally found in one of two ways. First, some measure of the mesospheric winds, u, can be used with the observed

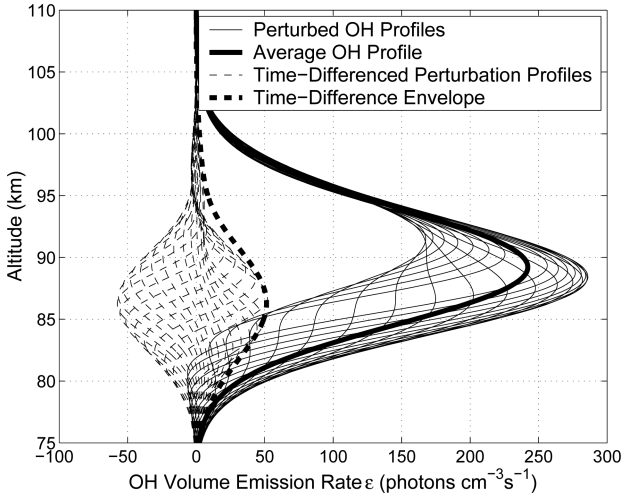

Fig. 2. Typical vertical profiles of a perturbed OH airglow layer. The thin solid lines represent a time-sequential series of a typical vertical emission profile perturbed 5% by a wave with a vertical wavelength of 25 km. The thick solid curve represents the average emission profile. The thin dashed curves represent the time-differenced perturbation profiles, while the thick dashed curve shows their envelope.

phase speed, c_o, to calculate c_i ($c_i = c_o - u$). The dispersion relation can then be used to find λ_z. Alternatively, λ_z can be inferred from simultaneous observations of two different airglow layers separated in altitude. Assuming that the wave has planar phase fronts and that the vertical separation of the layers is known, λ_z can be found by correlating the phase of the wave in each layer [9]. Deducing the amplitude of the wave requires the use of a cancellation factor, introduced in [8]. The cancellation factor relates the actual wave amplitude to the observable airglow perturbation amplitude and is a function of the specific airglow chemistry.

In general, the typical methods used to measure λ_z may not always be feasible. To use the dispersion relation, expensive laboratory equipment (along with the infrastructure required to operate it) is needed to measure mesospheric winds. Also, observing a wave in two layers may be challenging because of the 2π ambiguity of its phase or because it may only be visible in one layer owing to rapid, vertical wave dissipation or simply because it is ducted (i.e., the wave has no vertical propagation component).

An alternative method for determining the vertical wavelength is to use tomographic methods to reconstruct the vertical perturbation structure. This approach uses multiple-angle observations of an airglow perturbation from the ground to achieve a multidimensional view of the structure, allowing estimation of the vertical content.

The use of tomography in upper-atmospheric remote sensing has been widespread over the past few decades. One of the earliest and most applicable examples of ground-based atmospheric tomography is the use of ground-based radio receivers in the mid 1980s to measure ionospheric total electron count via orbiting satellites, using Faraday rotation and differential Doppler principles [10,11]. The imaging technique, called radio tomography, models the observation as a set of linear equations that are solved with the algebraic reconstruction technique. As the field of radio tomography grew, other reconstruction techniques were introduced. For example, Tikhonov regularization was used in [12,13], but instead of using an *a priori* model, the authors applied ionosonde and low-orbiting satellite measurements as inputs. In [14], the use of natural pixels (as opposed to square pixels) was used to represent the reconstruction object to set up a more sparse inverse problem. A stochastic framework for radio tomography inversion was reported in [15].

Recent advances in photometric and imaging technology has fueled many efforts to apply tomography to atmospheric emissions from both space-borne and ground-based observations. In [16], a concept was introduced that uses imaging spectroscopy to tomographically invert the spatial and spectral characteristics of auroral arcs. In [17,18], a stochastic-based regularization was applied to satellite data of extreme ultraviolet oxygen emissions in the ionosphere. Also, the algebraic reconstruction technique was applied in

optical tomography of satellite-limb measurements of the ionospheric 6300 Å emission as well as the three-dimensional reconstruction of an auroral arc from the 5577 Å oxygen emission observed by two cameras in Norway [19,20]. A nonlinear, general reconstruction method that parameterizes the reconstruction object first to a vertical profile function and then uses the result to initialize the multiplicative algebraic reconstruction technique was developed in [21]. This method was later applied in [22] to reconstruct the emission structure of a polar cap arc using data from two imagers in the Canadian arctic.

Despite the amount of research pertaining to atmospheric tomography, the works that deal with non-auroral mesospheric emission tomography remain relatively scarce. In [23,24], stochastic regularization principles were applied to a tomographic model and later to real data from two cameras. The result was a two-dimensional reconstruction from which the authors make the case that more imagers are needed to produce more accurate reconstructions. Later, a deterministic formulation to the problem was applied to show the potential for reconstruction using, again, a two-dimensional model [5].

The purpose of this paper is to develop the first tomographic model for data collected from an aircraft passing under the airglow structure. Using the assumption that the airglow structure does not change significantly over the course of the measurement, we may achieve a sufficient number (~13) of images to tomographically reconstruct it. This allows for a more complete projection set than what is feasibly provided by an array of ground-based imagers. We then apply this method to observations made during the airborne ALOHA-93 campaign.

The paper is organized by first describing the observation geometry and the associated assumptions. Next, the forward model is described followed by the inversion methodology. Then, a dataset is introduced and the described method is used to reconstruct the observed wave perturbations. We then substantiate our findings with the conclusions of another study of the same event [25]. Finally, we conclude the paper with a summary and closing remarks.

2. Observation Geometry

Our method applies tomographic techniques to airglow imagery that is gathered from an airborne platform. Over time, the aircraft can achieve multiple views of the airglow structure, providing the opportunity to tomographically estimate its vertical structure. In this section, we describe the specifics of the observation geometry and the associated assumptions.

The observation sensor is a spectroscopic imager that is mounted on an airborne platform, illustrated in Fig. 3. In this geometry, the collected data represent a series of fan-shaped projections from the imager. In this initial work, we consider only one row of pixels in each image such that we obtain a two-dimensional tomographic reconstruction representing a vertical slice of the airglow perturbation in the direction of the aircraft velocity.

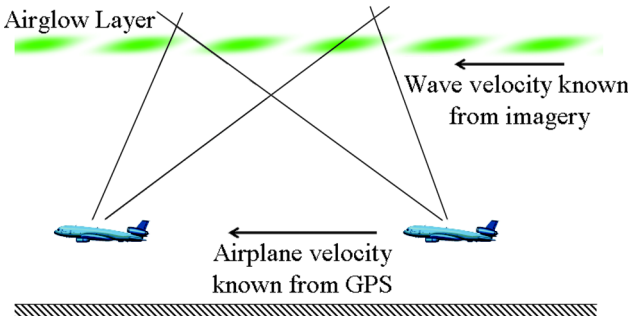

Fig. 3. Diagram of observation geometry. As the airplane travels under the airglow, it achieves multiple angle looks of a slow-moving airglow structure, allowing the possibility of tomographic reconstruction.

To support this geometry, we list four primary assumptions about the airglow structure and the airborne platform. First, we assume that within the time frame of the acquisition interval, the airglow structure does not change significantly. This is a reasonable assumption for perturbations of single waves or packets of waves with the same horizontal velocity because, within the typical acquisition intervals of ~20 min, the perturbation structure appears to change only in horizontal position and not shape. Second, we assume that the platform is at a high enough altitude (>5 km) that we can neglect extinction of the airglow due to atmosphere. This assumption is reasonable considering that the aircraft flies above most of the tropospheric constituents that are the dominant components in the extinction of ground-based atmospheric measurements. Third, we assume that the aircraft orientation is held steady over the course of the acquisition such that there are no changes to aircraft roll, pitch, or yaw.

Our last assumption is the altitude of airglow perturbations. The height of the OH perturbation layer has been extensively studied through modeling and satellite measurements [4,8,26], where the variability due to gravity waves and atmospheric tides has been shown to be consistent with the thick dashed curve in Fig. 2. As such, we assume that the vertical perturbation envelope is centered at 87 km. This assumption is important because mesospheric winds and AGW propagation are expected to significantly shift the horizontal position of the structure over the course of the observation, introducing ambiguity in the estimated height of the layer. By assuming the altitude, we avoid this ambiguity and are able to measure the observed horizontal phase speed from the dataset.

3. Preprocessing of Airglow Data

In practice, ground-based airglow imagery contains other artifacts of the nighttime sky that we count as image clutter, such as light contamination from stars and the Milky Way. However, we can use this clutter to make angle-to-pixel characterizations of

the imager to better understand how the data relate to the perturbation structure. Here, we describe the preprocessing steps taken before the tomographic reconstruction.

A. Pixel-to-Angle Map

Because the accuracy of the pixel-to-angle mapping is critical for tomography, we analyze the star field in one image to measure the sensor pixel-to-angle conversion. We first use sensor location (either from the GPS or a map) and acquisition time information to determine the appropriate star map for a given image. Next, we identify several stars in the image that span the entire field of view of the sensor. We then use nonlinear regression to fit the pixel locations of the stars to their respective angular locations in the sky, using the following constraining equations:

$$\begin{bmatrix} x_p \\ y_p \end{bmatrix} = \frac{1}{A} \begin{bmatrix} \cos(R) & \sin(R) \\ -\sin(R) & \cos(R) \end{bmatrix} \begin{bmatrix} e\ \sin(a) \\ e\ \cos(a) \end{bmatrix} + \begin{bmatrix} x_o \\ y_o \end{bmatrix}, \tag{1}$$

where x_p and y_p are the pixel coordinates of the stars, A is the instantaneous field of view of the sensor, a and e are, respectively, the star's azimuth and 90° complement of elevation, R is the angular rotation of the imager, and x_o and y_o are the coordinates of the zenith pixel.

B. Median Filtering and Time Differencing

The presence of clutter contamination in an image without proper treatment makes tomographic inversion extremely difficult if not impossible. To remove some of this contamination (along with some sensor noise), we apply a 3×3 median filter to the imagery to remove some of the stars in the image. To highlight the propagating airglow structure in the imagery, we use a two-point, temporal high-pass filter on the data. This filter effectively removes background features in the imagery, such as the unperturbed airglow emission and stellar contamination, and preserves the fast-moving wave perturbation structure. The simple time-filtering scheme amounts to nothing more than a frame-to-frame subtraction of the imagery, creating a series of time-differenced images.

Because the wave structure is strongly monochromatic, the choice of time interval (Δt) for the interframe subtraction makes a difference. Depending on the phase speed relative to the imager, Δt can either highlight the wave a lot, a little, or none at all because of the 2π redundancy of the wave. Since the imager is mounted to an aircraft, the velocity of the aircraft is added to the phase velocity such that the effective Δt on an aircraft can be much longer (or shorter) than it would be from the ground (with zero imager velocity).

4. Forward Model

The OH menial band results from the combination of hydrogen with ozone to produce OH in an excited energy state and diatomic oxygen. The OH molecule relaxes to a lower energy state by emitting a photon, whose spectrum is well studied [27]. Within the chosen spectral regions of the mesospheric airglow emissions, the optical transmission in the mesosphere is high, such that the airglow photons propagate freely with negligible absorption or scatter within the layer. For this reason, we consider the layer to be optically thin, so that the contribution of the airglow to a pixel's value on the ground can be considered a line integral along the observed slant path. A mathematical representation of this contribution can most simply be expressed as a line integral of the perturbation along the line of sight:

$$g(x,\theta) = A \int_0^\infty \gamma(\theta) f(l,x,\theta) \mathrm{d}l, \tag{2}$$

where $g(x,\theta)$ is the value of the pixel brightness due to the airglow, A is a constant photometric conversion factor, $\gamma(\theta)$ is the atmospheric transmittance along the line of site, l is a coordinate on the line coinciding with the pixel's line of site, and $f(l,x,\theta)$ is the emission line that lies along the pixel's line of site. The pixel value, $g(x,\theta)$, is a function of x and θ to signify the staring angle of the pixel (elevation angle of θ) and the horizontal coordinate x of the imager at the time of observation. Because the aircraft flew at an altitude of about 6450 m above sea level, well above the most significant tropospheric constituents contributing to atmospheric extinction, we assume that the transmittance function $\gamma(\theta) \approx 1$ for all angles and can therefore be ignored.

As a photometric conversion factor, A converts radiometric units to a pixel value. Since we are only interested in the structure of the airglow perturbations, we do not care about its absolute brightness and leave the reconstruction in arbitrary units. We, therefore, also discard A, so that Eq. (2) becomes

$$g(x,\theta) \approx \int_0^\infty f(l,x,\theta) \mathrm{d}l. \tag{3}$$

In practice, we discretize the problem and expand $f(l,x,\theta)$ into a set of orthonormal basis functions, $\phi_j(l,x,\theta)$, corresponding to the perturbation object's discretization:

$$f_J(l,x,\theta) = \sum_{j=1}^{J} f_j \phi_j(l,x,\theta), \tag{4}$$

where f_j are the discrete values of the object. For our application, we discretize the object based on our *a priori* knowledge of the perturbation feature size and the resolution supported by the data. At the very least, we would like to resolve the wave structure seen in the imagery. Typical horizontal wavelengths of AGWs are >20 km, and we desire an image resolution that supports their observation. Further, there is a limitation to the physical resolution of the airglow

structure brought about by the finite integration time of the sensor. Because the sensor is mounted to a fast-moving aircraft, the finite integration time (typically ~60) effectively blurs the airglow structure. Ultimately, how we discretize the object is based on these considerations.

Substituting Eq. (4) into Eq. (3),

$$g(x,\theta) \approx \sum_{j=1}^{J} f_j \int_0^{\infty} \phi_j(l,x,\theta)\mathrm{d}l. \tag{5}$$

The integral in Eq. (5) amounts to the length of the line segment passing through the area subtended by f_j. Therefore, $g(x,\theta)$ can be represented as a summation of each discretized emission value times its respective overlaying line segment. Thus, we achieve the overall system equation

$$\mathbf{g} = \mathbf{A}\mathbf{f}, \tag{6}$$

where $\mathbf{A}$ is called the projection matrix and contains the lengths of the line segments.

5. Problem Inversion

A. Formulation

The solution to Eq. (6) can be formulated as a least-squares minimization of a weighted vector norm. Unfortunately, because $\mathbf{A}$ is generally ill conditioned and because our data are noisy, the problem requires further constraint. We therefore regularize the inversion in order to penalize undesirable solutions.

Our classification of undesirable solutions rests on two assumptions. First, we expect the wave structure to be smooth, possessing no discontinuities. Second, we expect the perturbation structure to be confined to an altitude layer such that the perturbations are subject to some vertical envelope (as shown by the thick dashed curve in Fig. 2). Both of these assumptions are enforced with Tikhonov regularization.

Many papers assume either a Gaussian or similar shape to characterize the vertical envelope. In this work, we do not assume a specific envelope function but estimate it from the data. We propose a two-step process in which the first step is used to heuristically estimate the vertical envelope of the airglow perturbations and the second step is used to apply that estimate as another constraint on the solution.

Step 1: The solution to Eq. (6) can be formulated as a least-squares minimization of the error function, $J(\hat{\mathbf{f}})$, defined as

$$J(\hat{\mathbf{f}}) = \|\mathbf{g} - \mathbf{A}\hat{\mathbf{f}}\|^2 + \alpha^2\|\mathbf{D}\hat{\mathbf{f}}\|^2 + \beta^2\|\hat{\mathbf{f}} - \mathbf{H}\hat{\mathbf{f}}\|^2_{W_1}, \tag{7}$$

where $\hat{\mathbf{f}}$ is a vector containing the quantized elements of the reconstruction, α and β are regularization parameters, $\|\cdot\|^2$ denotes L^2 norm, $\mathbf{D}$ is a matrix that computes the gradient, $\mathbf{H}$ is a matrix that computes the average of all object values with the same altitude coordinate, and W_1 is the weighting:

$$W_1 = \begin{cases} 1 & \text{on the vertical bounds} \\ 0 & \text{else.} \end{cases} \tag{8}$$

The minimization of Eq. (7) produces a least-squares solution subject to two constraints. The first constraint penalizes large gradients in the solution, effectively dictating the smoothness of the reconstruction. The second constraint imposes extra horizontal smoothness along the highest and lowest altitude cells of the object. Because W_1 weights only the upper and lower altitude bins of the object, the second constraint penalizes only the deviations of upper and lower altitude object values from their horizontal averages. These are boundary conditions that specify that there should be no perturbations at those altitude bins and that the entire structure is confined within those boundaries.

The minimization of Eq. (7) is accomplished with the following estimate:

$$\hat{\mathbf{f}} = (\mathbf{A}^T\mathbf{A} + \alpha^2\mathbf{D}^T\mathbf{D} + \beta^2(\mathbf{I}-\mathbf{H})^T\mathbf{W}_1(\mathbf{I}-\mathbf{H}))^{-1}\mathbf{A}^T\mathbf{g}. \tag{9}$$

Step 2. The result of Eq. (9) is used to heuristically estimate the vertical envelope $p(z)$ of the airglow perturbations. This is done by analyzing the vertical weights imposed onto a single, prominent phase front, offering a direct measure of the vertical envelope. Our estimation of this quantity can then be applied to the rest of the object by adding a third side constraint to the error function:

$$J(\hat{\mathbf{f}}) = \|\mathbf{g} - \mathbf{A}\hat{\mathbf{f}}\|^2 + \alpha^2\|\mathbf{D}\hat{\mathbf{f}}\|^2 + \beta^2\|\hat{\mathbf{f}} - \mathbf{H}\hat{\mathbf{f}}\|^2_{W_1} + \mu^2\|\hat{\mathbf{f}} - \mathbf{H}\hat{\mathbf{f}}\|^2_{W_2}, \tag{10}$$

$$W_2 = \frac{1}{p(z) + 0.01} \tag{11}$$

for every altitude coordinate z in $\hat{\mathbf{f}}$. In this weighting function, $p(z)$ is the estimated vertical envelope and is normalized such that its maximum value is one. We choose the value of 0.01 in the denominator as an arbitrarily small number to avoid instability in W_2.

The two steps outlined in this section are used to constrain the solution to a vertical profile that is exactly known from only the data. In reality, there have been numerical reconstruction methods developed that may be applied to this problem in only one step. However, the application of these methods would likely require the use of an iterative optimization procedure to obtain a solution. The advantage of using the two-step process outlined in this section is that the inversion remains linear. Because of this, the reconstruction is not reached iteratively, and no stop or start criteria for the iteration is needed.

B. Choice of Regularization Parameters

The regularization parameters control the influence of their associated side constraints on the reconstruction.

If the parameter values are too low, the reconstruction depends too much on the data and may exhibit characteristics that are unphysical or go against *a priori* knowledge of the object. If the parameters are too high, the reconstruction is overregularized and is insufficiently influenced by the data. Four of the most common deterministic methods for choosing the regularization parameters include generalized cross validation, the discrepancy principle, the L-curve, and visual inspection [28]. With generalized cross validation, a parameter is chosen that minimizes the set of prediction errors. Unfortunately, this only works with decorrelated prediction errors, which does not apply to our case. The discrepancy principle requires that we know the bound of our prediction error, which, to an accurate extent, we do not. This leaves the L-curve and visual inspection as possibilities for our parameter choice. While the goal of the L-curve method is to objectively balance the influence that the data and the regularization have on the solution, visual inspection allows us to incorporate subjective prior knowledge of the object. For our application, we use both visual inspection and the L-curve to choose our parameters, depending on each step.

In the first step, our side constraints are chosen to determine the vertical envelope of the perturbation structure. We have two side constraints for this [see Eq. (7)]: one that imposes boundary conditions in the altitude, controlled by β, and one that imposes smoothness on the object, controlled by α. We set β to be a high value ($\sim$1000) to impose strict boundary conditions on the vertical envelope. We also expect the vertical envelope to be smooth, as supported by modeling and satellite observations [4,26]. In order to achieve a smooth estimate of the vertical envelope, the intermediate reconstruction must be smooth. With this in mind, we choose a value of α that extends beyond the elbow of the L-curve in favor of regularization. In our simulations, the elbow occurs for $\alpha \approx 15$; we choose to set $\alpha = 200$ for Step 1.

In Step 2, we apply the vertical envelope estimated from Step 1 to the reconstruction by means of a third side constraint. Here, we use visual inspection to choose values for α and μ. It just so happens that these values also fall very close to the elbow on the L-curve, validating our confidence in the choices. We still use a high value for β to enforce boundary conditions. In our simulations, we set $\alpha = 15$, $\beta = 1000$, and $\mu = 10$ for Step 2.

6. Experimental Results

In this section, we describe the application of our reconstruction method to an experimental dataset. We then show the resulting reconstructions and validations.

A. The Dataset

In the Fall of 1993, the National Center for Atmospheric Research Electra aircraft was used to observe mesospheric gravity wave activity by means of a Na–Rayleigh–Raman lidar, airglow imager, grating spectrometer, and Michelson interferometer. The flights were part of the ALOHA (Airborne Lidar and Observations of the Hawaiian Airglow) campaign and focused on studies of middle atmospheric dynamics and sporadic layer phenomena. During the experiment, more than 125 h of airborne observations were made of the mesospheric airglow layers, including those from an airglow imager outfitted with an optical filter to enhance contrast from either the hydroxyl (OH), sodium (Na), or molecular oxygen (O_2) emissions [29].

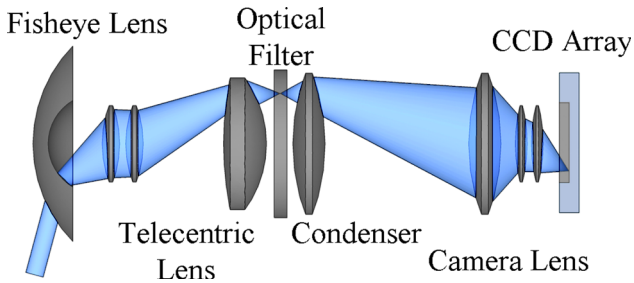

Fig. 4. Diagram of optics. The all-sky image is passed through the optical interference filter via telecentric optics, which minimize the incident angle of the oblique rays on the filter [30].

The optics, as shown by the diagram in Fig. 4, captured a hemispherical field of view. The optical design, introduced in [30], makes use of telecentric optics to ensure that the spectral response of the system is independent of field angle. As such, all the rays that passed through the filter were confined to a minimum incidence angle, making the system able to spectroscopically image a wide field in very narrow spectral regions. The imager was a 1024×1024 Loral array cooled to -50°C and was run in several binning configurations, which included a 3×3, 4×4, and 5×5 bin size, equating to an instantaneous field of view of 0.51, 0.68, or 0.86°/pixel, respectively.

We identified two datasets from the ALOHA-93 campaign for which the OH airglow structure remained fairly constant. In these datasets, the aircraft was flying in a direction opposite to the direction of wave propagation. The packet of AGWs in the imagery had the same apparent phase velocity such that the structure did not change shape with respect to the aircraft. The dataset numbers (designated by the authors) and measured event details are shown in Table 1. Relative to the Mount Haleakala observatory on Maui, run 15 occurred about 1600 km NE and run 38 occurred about

Table 1. Run Parameters

Parameter	Run 15	Run 38
Acquisition times	25 September, ~1330 UT	9 October, ~823 UT
No. of difference images	7	13
Look angle range	~110°	~125°
Observed phase speed	125 m/s	70 m/s
Propagation direction	60° E of N	30° E of S

Table 2. Highlighted Wavelengths Due to Time Differencing

Parameter	Run 15	Run 38
Δt	2.7 min	1.8 min
Distance wave traveled with respect to aircraft in Δt	~40 km	~22 km
λ_x with highest contrast	80 and 27 km	44 and 15 km
λ_x with lowest contrast	40 and 20 km	22 and 11 km

960 km NNW. The data from runs 15 and 38 show evidence of two different massive wall waves, the latter of which has been the subject of several papers [25,31].

The choice of object resolution is made based on *a priori* knowledge of the perturbation feature size and the resolution supported by the data. The resolution supported by the data is twofold. First, the imagers need a finite integration time interval to collect an image, during which the aircraft is moving at ~8 km/min. The integration time used for the imagery in run 15 is 1 min, implying a physical limitation in resolution of 8 km for a stationary wave with zero wind. Run 38 imagery was integrated for 20 s, implying a resolution limitation of 2.7 km. Second, we must consider the instantaneous field of view of the imagers. The resolution of the imagers in run 15 correspond to a 0.76 km horizontal sampling period of the airglow at zenith angles, while run 38 corresponds to a 1.2 km sampling period at zenith. Since the waves we are interested in reconstructing, which are ultimately observed and verified in the imagery, contain wavelengths >20 km, we discretize the object such that those features are accurately represented in the reconstruction.

Because of the 2π redundancy, some of the wave structure may not be completely preserved in the time differencing of the imagery. In fact, the choice of Δt for the time differencing will provide high contrast for some waves and low contrast for others. For this dataset, we set Δt at its minimum, corresponding to the time lapse between each frame. Given the observed phase speed of the waves and the aircraft velocity, in Table 2 we show which horizontal wavelengths will be highlighted the most and the least because of the time differencing.

B. Simulations

To promote a better understanding of the results, we present reconstructions of two simulated waves using the same projection matrix as used for the run 38 reconstruction. These waves have the same intrinsic properties (amplitude, λ_x, λ_z, and phase) as two waves observed in the run 38 results. Further, we add noise to the simulated data comparable with that on the real data.

The first simulated wave perturbation is shown in the top panel of Fig. 5, where a monochromatic wave with $\lambda_x = 40$ km and $\lambda_z = 25$ km is enveloped by a Gaussian vertical profile. The reconstruction of this simulated perturbation is shown in the bottom panel of Fig. 5. The second simulated wave perturbation is shown in Fig. 6. This wave has $\lambda_x = 175$ km and $\lambda_z = 22$ km and the same vertical profile. Note the degradations on the right-hand sides of both reconstructions indicating limited support from the projection geometry at those regions. Also, the black pixels on the lower corners of the reconstructions indicate regions of no support from the geometry.

Simulations using the run 15 projection matrix yield similar results. This is expected given the similarity of the projection matrices for runs 15 and 38.

C. Results

Figure 7 shows a subset of the time difference images used for both reconstructions. Figures 9 and 10 show the reconstructed slices of the perturbation functions. Again, the black pixels in the object are pixels that have no representation from the data. The plot in Fig. 8 shows a comparison of the projected reconstruction with the data. Even though the two curves are similar, there is a clear deviation of the projected reconstruction from the data. This is actually the function of our choice in regularization: to deviate from the data in favor of our prior knowledge of the object.

D. Substantiation of Results

The primary benefit to performing tomography on mesospheric airglow is to determine the vertical wavelength of the waves passing through. Our reconstructions show clear evidence of wave activity. In

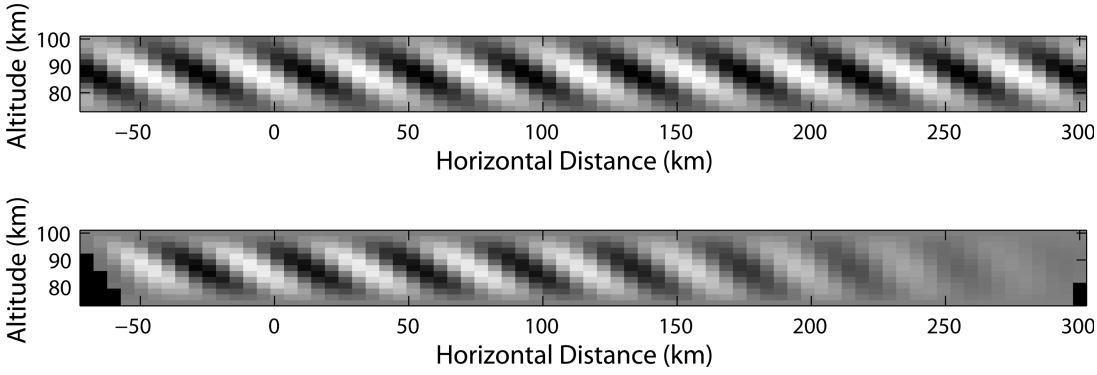

Fig. 5. Reconstruction of a simulated wave perturbation with $\lambda_x = 40$ km and $\lambda_z = 25$ km. Top panel, original simulated perturbation; bottom panel, reconstruction.

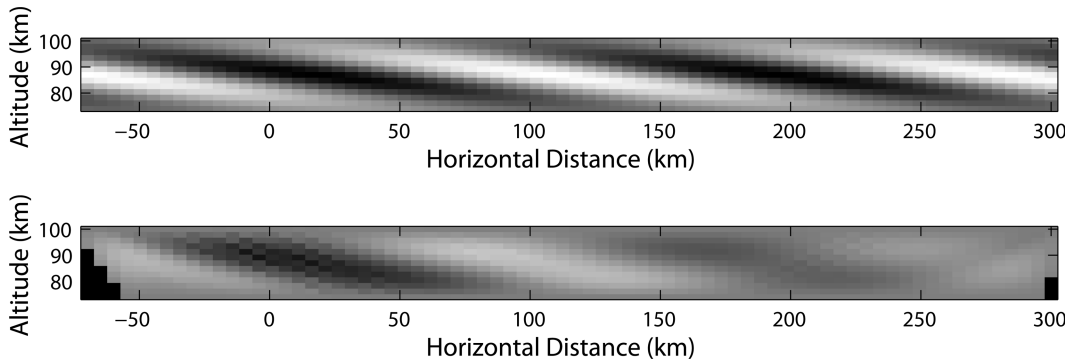

Fig. 6. Reconstruction of a simulated wave perturbation with $\lambda_x = 175\,\text{km}$ and $\lambda_z = 22\,\text{km}$. The top panel shows its original simulated perturbation; the bottom shows its reconstruction.

this section, we substantiate the observed wave characteristics by checking their consistency with known AGW parameters.

We first make the important observation that the wave structure in both runs does not change shape over the course of acquisition. This implies that the waves that make up the structure are moving together and have the same intrinsic phase speed. This is important because if the reconstructions show evidence of multiple waves, then they have the same phase velocity, and thus their vertical and horizontal wavelengths are linked by the dispersion relation. With this understanding, we are able to test whether the observed waves are at least consistent with each other.

The reconstruction of run 38 in Fig. 10 shows two distinct waves. In comparison with the simulated waves in Figs. 5 and 6, the phase fronts identified in Fig. 10 are in regions of the reconstruction that appear to be well supported by the projection geometry such that λ_z can be estimated. One wave has an apparent horizontal wavelength of ∼175 km and a vertical wavelength of ∼22 km, as shown in the rescaled reconstruction image in the middle panel of Fig. 10. In the image, the two lines lie along an apparent phase front and highlight one half of a cycle. The dashed line lies in a trough of the wave, and the solid line lies along a peak. According to the dispersion relation, this wave has an intrinsic phase speed of ∼67 m/s. The second wave is highlighted in the bottom panel of Fig. 10. In this figure, two solid lines lie along the phase front to show a full oscillation. Our observations of this wave indicate that this wave has a horizontal wavelength of ∼40 km and a vertical wavelength of ∼25 km. The intrinsic phase speed related to this wave is also ∼67 m/s.

Further, because the event in run 38, called the October 9 wall wave, was extensively studied in [25] via data from the Na lidar, we are provided with another check for the tomographic observations. In the study, it was found that the fundamental wave associated with this event had a horizontal wavelength of

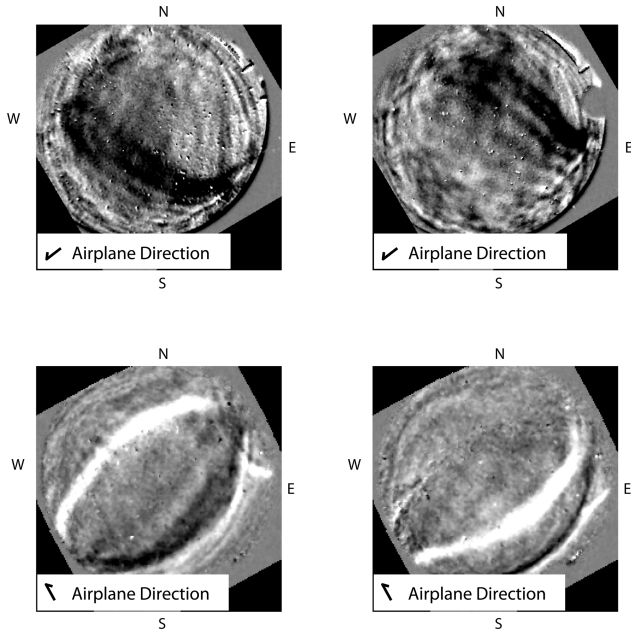

Fig. 7. Time difference images for the two datasets: The top two are from run 15; the bottom two are from run 38.

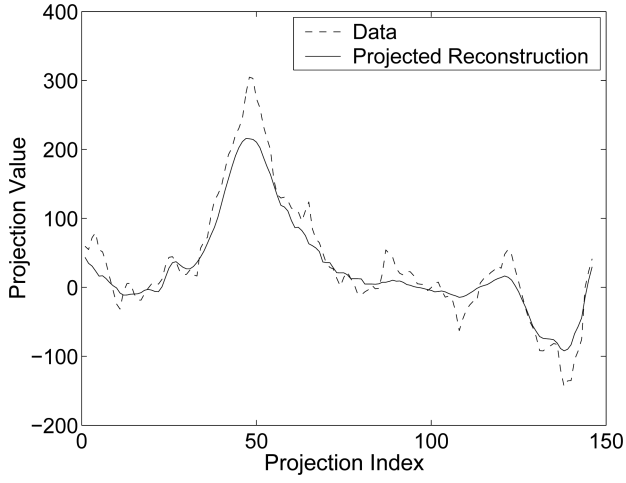

Fig. 8. Comparison of one projection of the run 38 reconstruction to the data. The reconstruction is mostly consistent with the data, but small deviations do exist due to our choices in regularization.

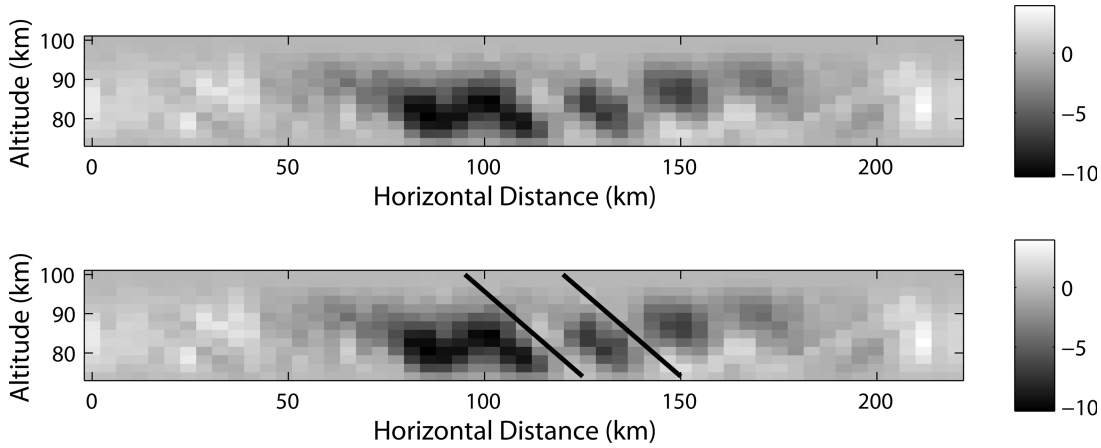

Fig. 9. Run 15 perturbation preconstruction. The lines in the bottom panel show two phase fronts of a wave with ~25 km for both horizontal and vertical wavelengths. These particular wavelengths are some of the most commonly observed in airglow [32].

~350 km and a vertical wavelength of 20 km (invisible to the airglow imager). Further, it is reported that the intrinsic phase speed of the lidar-observed wave is 66 m/s, approximately what we observe from the wave packet in the reconstruction of the same event. This comparison gives context to the two waves observed in the reconstruction and shows their consistency with lidar observations.

In run 15, one wave clearly stands out as shown by the lines in the bottom panel of Fig. 9. Unfortunately, we have no supporting data on the characteristics of this wave. However, we note that the phase fronts appear in a region of the solution space that is well supported by the projection geometry and that the wave parameters observed in the reconstruction (both horizontal and vertical wavelengths ~25 km) are those most commonly observed in mesospheric airglow [32].

7. Conclusion

In this paper, using a single, aircraft-mounted spectroscopic imager, we develop a method for tomographically reconstructing the perturbations imparted to mesospheric airglow layers by atmospheric gravity waves. As the aircraft passes under the airglow, it collects multiple-angle views of the perturbation structure. Under the assumption that the airglow structure does not change significantly over time, the resulting data can be tomographically reconstructed to estimate vertical wave information. After developing the methodology, we use it to compute tomographic reconstructions for two data sets from the ALOHA-93 campaign. The resulting reconstructions show clear vertical structure in the airglow layers that is well supported by the data. Also, the waves seen in our reconstruction in run 38 have been found

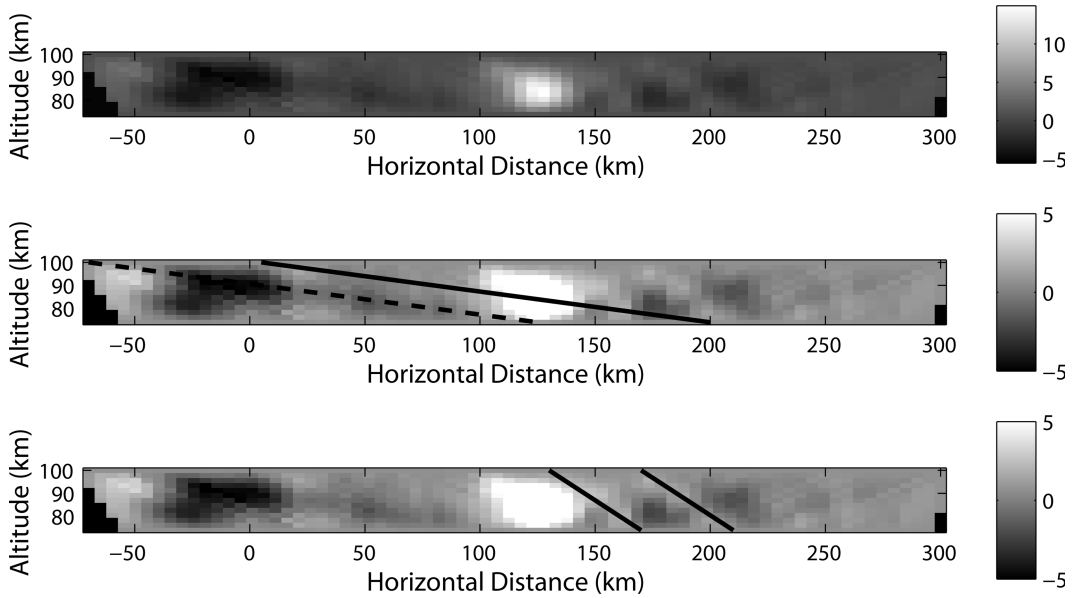

Fig. 10. Run 38 perturbation reconstruction. The bottom two are contrast-enhanced and highlight two phase fronts that have the same observed phase speed. The dispersion relation supports that these waves intrinsically propagate at the same speed, indicating the internal consistency of the reconstruction.

to be consistent with lidar studies of that event. Further, the parameters of the waves observed in run 15 are typical for waves observed in previous studies. The method described here has been developed for data acquired from an airborne platform. However, this method is directly applicable to nadir and slant path viewing of the airglow perturbations from spacecraft. From this perspective, the global mapping of gravity wave effects can be investigated.

This work was supported by the National Science Foundation under grants ATM 01-35073 and ATM 05-45704 to the University of Illinois.

References

1. C. O. Hines, "Internal atmospheric gravity waves at ionospheric heights," Can. J. Phys. **38**, 1441–1481 (1960).
2. J. R. Holton, "The role of gravity wave induced drag and diffusion in the momentum budget of the mesosphere," J. Atmos. Sci. **39**, 791–799 (1982).
3. R. A. Vincent, "Gravity-wave motions in the mesosphere," J. Atmos. Terr. Phys. **46**, 119–128 (1984).
4. A. Z. Liu and G. R. Swenson, "A modeling study of O_2 and OH airglow perturbations induced by atmospheric gravity waves," J. Geophys. Res. **108**, ACH 11-1 (2003)..
5. G. Swenson, J. Tang, F. Kamalabadi, and S. Frank, "Methods of deducing intrinsic measurements of high frequency Atmospheric Gravity Waves (AGWs)," in Proc. SPIE **5979**, 59790V (2005).
6. M. J. Taylor, D. C. Fritts, and J. R. Isler, "Determination of horizontal and vertical structure of an unusual pattern of short-period gravity waves imaged during ALOHA-93," Geophys. Res. Lett. **22**, 2837–2840 (1995).
7. J. Tang, G. R. Swenson, A. Z. Liu, and F. Kamalabadi, "Observational investigations of gravity wave momentum flux with spectroscopic imaging," J. Geophys. Res. [Atmos.] **110** (2005).
8. G. R. Swenson and C. S. Gardner, "Analytic models for the responses of the mesospheric OH^* and Na layers to atmospheric gravity waves," J. Geophys. Res. **103**, 6271–6294 (1998).
9. F. Vargas, G. R. Swenson, A. Z. Liu, and D. Gobbi, "$O(^1S)$, OH, and $O_2(b)$ airglow layer perturbations due to AGWs and their implied effects on the atmosphere," J. Geophys. Res. [Atmos.] **112** (2007).
10. J. R. Austen, S. J. Franke, C. H. Liu, and K. C. Yeh, "Application of computerized tomography techniques to ionospheric research," in *International Beacon Satellite Symposium on Radio Beacon Contribution to the Study of Ionization and Dynamics of the Ionosphere and to Corrections to Geodesy and Technical Workshop, Proceedings. Part 1*, A. Taurianinen, ed. (International Union of Radio Science, 1986), pp. 25–35.
11. J. R. Austen, S. J. Franke, and C. H. Liu, "Ionospheric imaging using computerized tomography," Radio Sci. **23**, 299–307 (1988).
12. G. C. Fehmers, L. P. J. Kamp, F. W. Sluijter, and T. A. T. Spoelstra, "A model-independent algorithm for ionospheric tomography 1. Theory and tests," Radio Sci. **33**, 149–163 (1998).
13. G. C. Fehmers, L. P. J. Kamp, F. W. Sluijter, and T. A. Spoelstra, "A model-independent algorithm for ionospheric tomography 2. Experimental results," Radio Sci. **33**, 165–173 (1998).
14. J. Semeter and F. Kamalabadi, "A natural pixel decomposition for tomographic imaging of the ionosphere," *Proceedings of the 1998 IEEE International Conference on Acoustics, Speech and Signal Processing, 1998* (IEEE Signal Processing Society, 1998), vol. **5**, pp. 2913–2916.
15. T. Nygren, M. Markkanen, M. Lehtinen, M. Tereshenko, and B. Z. Khudukon, "Stochastic inversion in ionospheric radiotomography," Radio Sci. **32**, 2359–2372 (1997).
16. G. R. Swenson, R. L. Rairden, S. C. Solomon, and S. Ananth, "Instrument for the monochromatic observation of all sky auroral images," Appl. Opt. **37**, 5760–5770 (1998).
17. F. Kamalabadi, W. C. Karl, J. L. Semeter, D. M. Cotton, T. A. Cook, and S. Chakrabarti, "A statistical framework for space-based EUV ionospheric tomography," Radio Sci. **34**, 437–447 (1999).
18. F. Kamalabadi, G. Bust, K. Dymond, S. Gonzalez, P. Bernhardt, S. Chakrabarti, D. Cotton, A. Stephan, R. McCoy, S. Budzien, and S. Thonnard, "Tomographic studies of aeronomic phenomena using radio and UV techniques," J. Atmos. Sol.-Terr. Phys. **64**, 1573–1580 (2002).
19. S. Frey, H. U. Frey, D. J. Carr, O. H. Bauer, and G. Haerendel, "Auroral emission profiles extracted from three-dimensionally reconstructed arcs," J. Geophys. Res. **101**, 21,731–21,741 (1996).
20. S. Frey, S. B. Mende, and H. U. Frey, "Satellite limb tomography applied to airglow of the 630 nm emission," J. Geophys. Res. **106**, 21367–21380 (2001).
21. J. Semeter and M. Mendillo, "Nonlinear optimization technique for ground-based atmospheric emission tomography," IEEE Trans. Geosci. Remote Sens. **35**, 1105–1116 (1997).
22. R. A. Doe, J. D. Kelly, J. L. Semeter, and D. P. Steele, "Tomographic reconstruction of 630.0 nm emission structure for a polar cap arc," Geophys. Res. Lett. **24**, 1119–1122 (1997).
23. T. Nygren, M. J. Taylor, M. S. Lehtinen, and M. Markkanen, "Application of tomographic inversion in studying airglow in the mesopause region," Ann. Geophys. **16**, 1180–1189 (1998).
24. T. Nygren, M. J. Taylor, G. R. Swenson, and M. S. Lehtinen, "Observing gravity wave activity in the mesopause region by means of airglow tomography," Adv. Space Res. **26**, 903–906 (2000).
25. G. R. Swenson, J. Qian, J. M. C. Plane, P. Espy, M. J. Taylor, D. N. Turnbull, and R. P. Lowe, "Dynamical and chemical aspects of the mesospheric Na 'wall' event on October 9, 1993 during the Airborne Lidar and Observations of Hawaiian Airglow (ALOHA) campaign," J. Geophys. Res. **103**, 6361–6380 (1998).
26. R. Nikoukar, G. Swenson, A. Z. Liu, and F. Kamalabadi, "On the variability of mesospheric OH emission profiles," J. Geophys. Res. **112** (2007).
27. J. W. Chamberlain, *Physics of the Aurora and Airglow* (American Geophysics Union, 1995).
28. W. C. Karl, "Regularization in image restoration," in *Handbook of Image and Video Processing* A. Bovik, ed. (Academic, 2000), pp. 141–160.
29. "Special Section: ALOHA/ANLC-93," J. Geophys. Res. **103**, 6249–6481 (1998).
30. S. B. Mende, R. H. Eather, and E. K. Aamodt, "Instrument for the monochromatic observation of all sky auroral images," Appl. Opt. **16**, 1691–1700 (1977).
31. G. R. Swenson and P. J. Espy, "Observations of 2-dimensional airglow structure and Na density from the ALOHA, October 9, 1993 'storm flight'," Geophys. Res. Lett. **22**, 2845–2848 (1995).
32. G. R. Swenson, M. J. Alexander, and R. Haque, "Dispersion imposed limits on atmospheric gravity waves in the mesosphere: observations of OH airglow," Geophys. Res. Lett. **27**, 875–878 (2000).